

The poloidal distribution of turbulent fluctuations in the Mega-Ampère Spherical Tokamak

G. Y. Antar

University of California, San Diego, 9500 Gilman Drive, La Jolla, California 92093-0417

G. Counsell, J.-W. Ahn,^{a)} Y. Yang,^{b)} M. Price, A. Tabasso, and A. Kirk

EURATOM/UKAEA Fusion Association, Culham Science Centre, Abingdon, Oxfordshire OX14 3DB, United Kingdom

(Received 5 October 2004; accepted 20 December 2004; published online 18 February 2005)

Recently, it was shown that intermittency observed in magnetic fusion devices is caused by large-scale events with high radial velocity reaching about 1/10th of the sound speed (called avaloids or blobs) [G. Antar *et al.*, *Phys. Rev. Lett.* **87** 065001 (2001)]. In the present paper, the poloidal distribution of turbulence is investigated on the Mega-Ampère Spherical Tokamak [A. Sykes *et al.*, *Phys. Plasmas* **8** 2101 (2001)]. To achieve our goal, target probes that span the divertor strike points are used and one reciprocating probe at the midplane. Moreover, a fast imaging camera that can reach 10 μ s exposure time looks tangentially at the plasma allowing us to view a poloidal cut of the plasma. The two diagnostics allow us to have a rather accurate description of the particle transport in the poloidal plane for *L*-mode discharges. Turbulence properties at the low-field midplane scrape-off layer are discussed and compared to other poloidal positions. On the low-field target divertor plates, avaloids bursty signature is not detected but still intermittency is observed far from the strike point. This is a consequence of the field line expansion which transforms a structure localized in the poloidal plane into a structure which expands over several tens of centimeters at the divertor target plates. Around the *X* point and in the high-field side, however, different phenomena enter into play suppressing the onset of convective transport generation. No signs of intermittency are observed in these regions. Accordingly, like “normal” turbulence, the onset of convective transport is affected by the local magnetic curvature and shear. © 2005 American Institute of Physics. [DOI: 10.1063/1.1861894]

I. INTRODUCTION

Since Langmuir probes were installed on magnetic fusion devices, transport in the scrape-off layer (SOL) was observed to be intermittent.^{1,2} To characterize this process different statistical tools were used. The probability distribution function showed clearly the deviation of the fluctuations from a Gaussian distribution.^{3,4} The frequency spectrum was often used to describe the power distribution across the different length scales.^{5,6} Other more sophisticated tools such as wavelet transforms,^{7,8} conditional analyses,⁹ and the Hurst parameter^{10,11} were also used to characterize intermittency.

Recently, in a series of publications,^{12–15} more progress is made in understanding the nature and the origin of intermittency in the scrape-off layer. This paper comes thus in continuation of this effort to have a rather comprehensive picture of the SOL properties.

In Ref. 12, we argued using different statistical methods that intermittency in the SOL of magnetic confinement devices is actually different from intermittency encountered in fully developed turbulence of neutral fluid systems.¹⁶ In neutral fluid, turbulence intermittency is caused by rare events that are locally organized driven by coherent vorticity.^{17,18} It

was shown by different groups that intermittency in turbulent flows occur at small scales that are close to the so-called Kolmogorov scale where kinematic dissipation starts to play an important role. In Ref. 12, we showed that in the SOL of fusion plasmas, intermittency comes from large-scale structures. By large scales, we mean scales close to or even bigger than the macroscopic scale of turbulence. Hence, although there may exist some similarities between intermittency in fluids and plasmas,⁴ the origin and effects are very much different in the two media.

In Ref. 13, we continued our investigation with two main goals. First is the determination of the bursts radial velocity, which turns out to be large reaching a fraction of the sound speed. The second goal was to assess the relative importance of these intermittent convective bursts and turns out to be important accounting for approximately half of the total particle radial transport. These results, performed on the PISCES linear device and the Tore Supra tokamak, were confirmed later on other devices such as the DIII-D tokamak.¹⁹ The new term, avaloids, was defined to denote large-scale plasma structures with high radial velocity encountered intermittently in the SOL. From this definition it is rather clear that avaloids are different from coherent structures. Avaloids do not require coherent vorticity whereas the coherent structures do. Moreover, coherent structures may not have large radial velocities whereas it is required for avaloids. The term blob is also used in the literature. How-

^{a)}Present address: College of Letters and Science, University of Wisconsin, 1150 University Avenue, Madison, WI 53706.

^{b)}Present address: Institute of Plasma Physics, Chinese Academy of Sciences, Hefei 230031, People's Republic of China.

ever, because it does not have a clear definition, it induces confusion as it might denote coherent structures of turbulence in the SOL or avaloids (originally, however, the terms blobs²⁰ and avaloids¹³ denoted the same intermittent structures found in the SOL).

In Ref. 14, we performed a comprehensive analysis using up to nine different statistical analyses, and four different magnetic confinement devices employing four different probe designs. All the data analyses yielded identical properties of the turbulent fluctuations in the SOL. It was logically deduced that avaloids are universal in the sense that they have more or less the same properties in magnetic fusion devices.

After showing the universality of avaloids, we turned to investigate their origin on the PISCES linear plasma device.¹⁵ We took advantage of the simple linear geometry and accessibility to Langmuir probes. We used multiple arguments to emphasize that avaloids, even though they are encountered intermittently, they are, however, emitted periodically or semiperiodically. We showed that avaloids in the far SOL are correlated to coherent oscillations inside the main plasma column in the PISCES linear device. We concluded that avaloids result from a nonlinear saturation of an instability that is taking place at the plasma edge.

Because avaloids are observed to have a higher density and temperature than the background in the far SOL, it is crucial to establish where do they occur in a toroidal device and thus how they affect the particle and the power distribution in the SOL. This issue is particularly important for future devices such as the International Thermonuclear Experimental Reactor (ITER). Even though future large fusion devices will most probably operate in high confinement mode regime (*H* mode), they will still need to go through a low confinement mode (*L* mode) stage. Therefore, it might be possible that the lifetime of the first wall would be dictated by the *L*-mode phase rather than the *H*-mode phase including edge localized modes (ELMs). Both avaloids and ELMs transport hot and dense matter into the far SOL, but one of the main differences between them is their frequency. Avaloids are reported to have a repetition rate of about 5 kHz that is more or less independent of several macroscopic plasma parameters.^{14,15} ELMs, on the other hand, have a frequency in the range of few hertz.²¹ Therefore, avaloids occur 1000 times more frequent than ELMs hence their importance.

Poloidal asymmetry in tokamaks was investigated in the past.^{22,23} It was shown that along the field lines turbulence intensity and its statistical properties are different depending on the poloidal angle. Mainly, the high-field vs low-field asymmetry is well established where the role of the curvature as a stabilizing/destabilizing effect were shown to be at the origin. The goal of this paper is to investigate the poloidal distribution of avaloids. This is performed on the Mega-Ampère Spherical Tokamak (MAST) using two main diagnostics. Langmuir probes that are distributed at different poloidal and radial locations in the tokamak are used. The second diagnostic is a fast imaging camera with an exposure time that can be set to as low as 10 μ s. The images are dominated by the D_α light allowing us to have a rather good

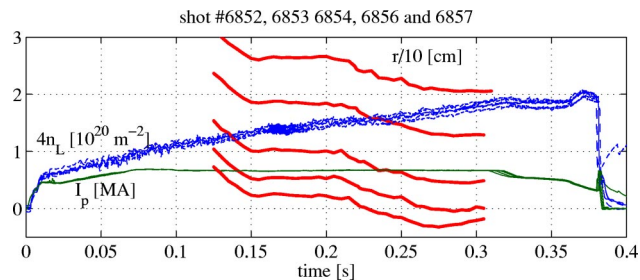


FIG. 1. The plasma current, the line-integrated density, and the probe position with respect to the LCFS for five plasma discharges that enable us to perform a detailed radial scan at the midplane while at the target this takes place naturally due to the strike motion during the discharge.

description of the poloidal distribution of avaloids without the need of specific gas puffing.

In the following section we detail the different diagnostics used and their properties. In Sec. III, the results obtained by Langmuir probes are discussed. Avaloids are shown to be poloidally asymmetric as they are observed to exist only at the low-field side. In Sec. IV, we use the fast imaging camera, which also gives us a good picture of what is happening on the low-field side. The poloidal asymmetry is shown not to depend on the magnetic configuration single or double null.

II. THE EXPERIMENTAL SETUP

The results presented in this paper were obtained on the MAST.²⁴ One of the main characteristics of MAST is the small aspect ratio R/a that is about 1.4, the major and minor radii of the plasma studied being, respectively, $R=0.73$ m and $a=0.52$ m. Top and bottom divertors in MAST allow different magnetic configurations. The results obtained here were taken in lower double null (LDN) divertor as well as the connected double null divertor (CDN) configurations. The LDN configuration describes a magnetic connection similar to a single null but with the upper *X* point not completely gone. The CDN configuration occurs where two *X* points on the top and bottom clearly exist. The gas used in our study is deuterium, and the main plasma parameters of these Ohmic *L*-mode discharges are the toroidal magnetic field 0.6 T, the plasma density 4×10^{19} m⁻³ and the plasma current 0.7 MA. In Fig. 1, the plasma current and the line-integrated density are plotted for five plasma discharges used in this paper.

Figure 2 shows an EFIT equilibrium reconstruction.²⁵ The center stack and the divertor plates are illustrated with thick solid vertical and horizontal lines. We also schematized the main diagnostics used to investigate the turbulent fluctuations poloidal distribution. Note the rather large field line expansion between the *X* point and the target plates. Therefore, a localized structure in the SOL at the midplane expands with approximately a factor of 5 increase at the target plates.

At the midplane of the low-field side, a reciprocating probe (RP) is used containing three sets of tips. A detailed plot of the probe design is included in Fig. 2. The diameter of each tip is 0.15 cm and the poloidal distance between two

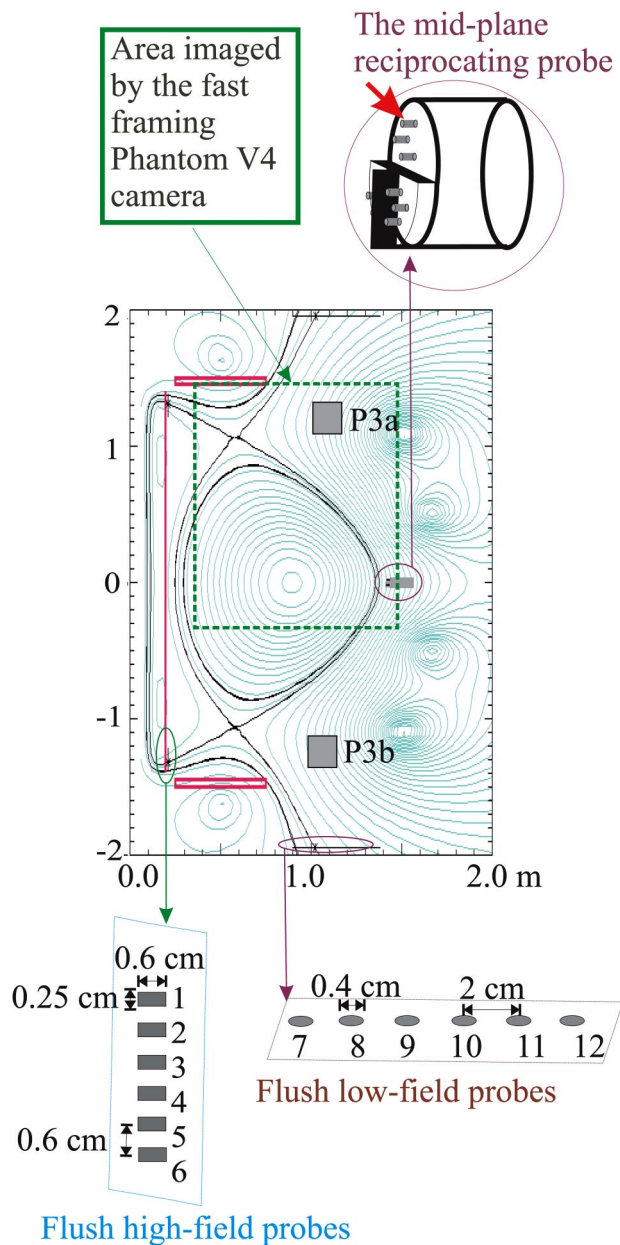


FIG. 2. A schematic of a poloidal plane cut of the MAST spherical tokamak where the x and y axes are in meters. The contour plots result from running the EFIT program. The solid contour lines indicate the last closed flux surface and the “*” sign shows the strike point position on the four divertor target regions. P3a and P3b are two magnetic coils. The dashed rectangle indicates the area imaged by the Phantom V4 fast camera. The schematic of the reciprocating probe is drawn where the tips are identical. They are cylinders with 0.15 cm in diameter and 0.31 cm in length. The target probes are divided into two groups: the high-field probes enumerated from 1 to 6 and the low-field probes enumerated from 7 to 12. The low-field side probes are inserted in the center stack, with 0.6 cm distance between them; their shape is rectangular. Two series of flush probes on the low-field side are installed on the top and bottom of the chamber. They are circular with 0.4 cm in diameter.

floating probes is 0.5 cm. In the radial direction the distance between the two sets of probes is 0.5 cm. For the purpose of this paper, however, one probe tip is used and is indicated by an arrow. The reciprocating probe position r with respect to the last closed flux surface (LCFS) was plotted in Fig. 1 for the four plasma discharges. The plasma motion causes the

variation of the probe position with respect to the LCFS while the RP is kept fixed. As one can notice, r can take values as high as 30 cm. Plasma can be detected up to that distance because MAST does not have a first wall close to the plasma.

MAST has 576 flush-mounted target probes (TP) positioned around the four strike point regions at the same toroidal angle. Here, we make use of only 12 tips that are biased to ion saturation current. They are chosen to be around the lower outer and the lower inner strike points. As it is the case for the reciprocating probe tip, the acquisition frequency is set to 1 MHz with a total number of points recorded for each tip equal to 180 000. The same trigger is used to start the acquisition on the reciprocating probe and the divertor target probes. The details of the different flush-mounted tips in the divertor targets are schematized in Fig. 2. The tips that are in the high-field side near the lower-inner or upper-inner strike points have a rectangular shape. The tips on the low field side near the lower-outer or upper-outer strike points are circular in shape. Hereafter, the ion saturation current density is used for data display. It is calculated by dividing the ion saturation current by the probes surface area. The current density, or the parallel particle flux, nc_s is referred to as the particle flux, where c_s is the speed of sound. By the radial particle flux, we designate nv_r , where v_r is the radial velocity.

The large rectangle in dashed line in Fig. 2 shows the area imaged by the fast camera. Looking tangentially at the plasma D_α light, it allows us to perform investigation of the poloidal fluctuations in a rather continuous fashion from the midplane to regions close to the X point. The fast imaging camera is a Phantom V4 type with 8 bits resolution. It is set to take images with 10 μ s exposure time at a rate equal to 2115 frames/s.

III. THE POLOIDAL PROPERTIES OF TURBULENCE USING ELECTRICAL PROBES

In this section, we use the probes around the MAST spherical tokamak to assess the poloidal properties of turbulence. It will be shown that the properties of turbulence are different at different poloidal locations, and avoids bursty signature is not clear at the target plates. In this section, we first show the raw ion saturation current density signals obtained at the midplane and at the divertor target plates. Then, we use statistical analyses to present a quantitative picture of the properties of turbulence as a function of the radial position for the different poloidal locations.

A. Turbulence at the midplane

In order to investigate the radial dependence of turbulence at the midplane the reciprocating probe is used. Five discharges with the same plasma parameters but with different positions of the RP are performed. This was illustrated in Fig. 1 where the plasma current and line-averaged density was shown along with the RP position to the LCFS. We recall that the discharges are Ohmically heated L -mode plasmas.

In order to show the radial profile, we included the ion saturation current density obtained during the four plasma

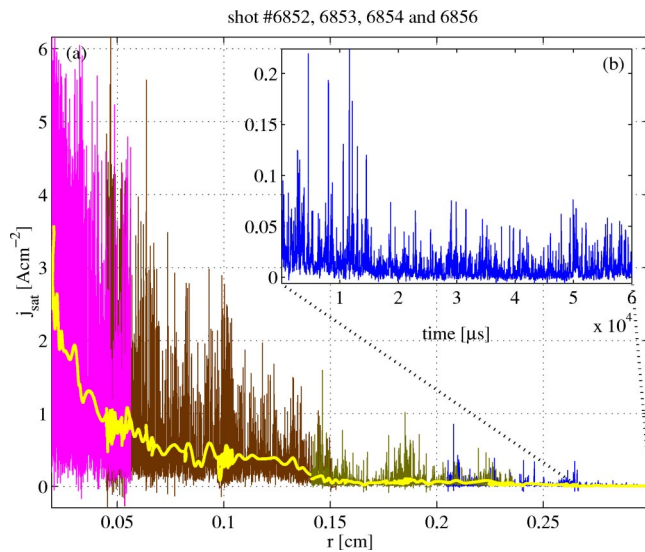


FIG. 3. The ion saturation current density as a function of the distance to the LCFS (r). Four identical plasma discharges were necessary to produce this graph. Note that for $r \sim 0$, the fluctuations are about the average value. As r increases, this is no longer true, and intermittent bursts appear to make high intensity bursts more probable. Avaloids are still present even at distances as far as 30 cm away from the LCFS. This is shown in the subplot (b) where we illustrate the time dependence of j_{sat} for r varying between 27 and 30 cm. The wiggles in the average value in (a) are caused by a stagnation of r about some position to the LCFS.

discharges. This is shown in Fig. 3 where also are plotted the average values of j_{sat} . Near the last closed flux surface, the fluctuations are around the average values in a rather symmetric fashion. In other words, negative and positive fluctuations around the mean value have approximately the same probability to occur. As the probe gets farther from the LCFS, the fluctuations become more and more asymmetric with respect to the average value. High intensity bursts, say at $r \sim 10$ cm, intermittently have current densities that are of the order of the average current density recorded at plasma edge. Although j_{sat} decreases in intensity as r increases, the subplot (b) of Fig. 3 clearly shows that plasma is still present in an intermittent fashion even at 30 cm away from the LCFS. These facts are in excellent agreement with the radial profile of j_{sat} performed on the PISCES linear device and published in Refs. 13 and 14. Avaloids are thus clearly present at the midplane of MAST. Their velocity was determined in Ref. 14 to be about 10^5 cm/s and their radial scale about 5 cm. They lead to plasma that exists far from the LCFS in an intermittent fashion in addition to the plasma caused by diffusive turbulence where the radial velocity is rather small.

B. Turbulence at the target plates

The plasma near the strike points in MAST was investigated in Refs. 26 and 27. The target probes applied voltage was swept rapidly and the density and temperature profiles at the divertor target regions were obtained in a LDN magnetic configuration. The electron density and temperature at the strike point were found to vary between 0.5 and $6 \times 10^{18} \text{ m}^{-3}$, and 10 – 20 eV, respectively. The decay on either side of the strike point was found to be exponential.

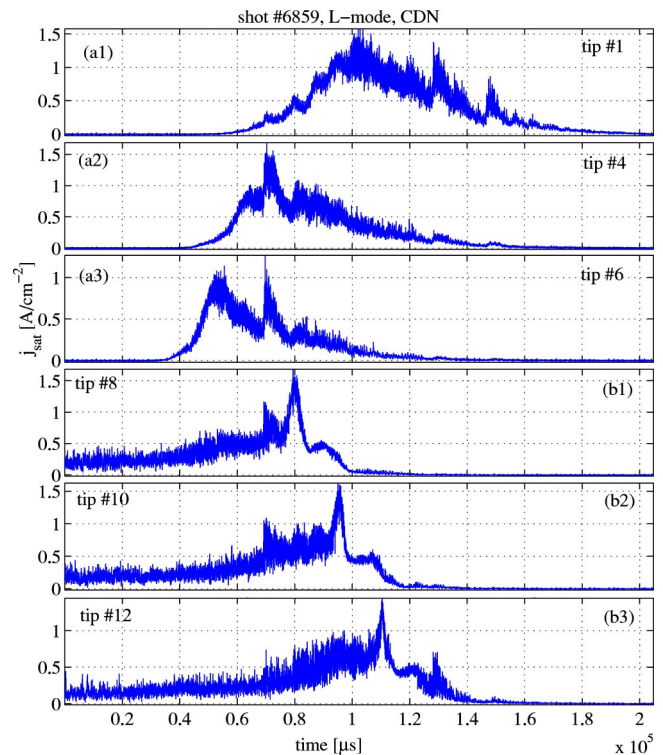


FIG. 4. The subplots (a1)–(a3) illustrate the ion saturation current density, acquired at 1 MHz, taken at the high-field divertor target probes. The strike point occurs first on tip 6, then 4, and then 1. On the low-field side, the strike point passes on tip 8, then 10, and then 12. Following the strike point position in time and knowing the distance among the probes, we deduce that the strike point velocity is about 2.7 m/s at the low-field side and about 0.7 m/s at the high-field side.

During the plasma discharge in MAST, the low-field strike points move outward away from the center stack. At the same time, the high-field strike points move towards the center. This result comes from the fact that the MAST solenoid is shorter than the vessel and close to the plasma due to the spherical tokamak geometry. In consequence, there is a large fringing field from the end of the solenoid. As the solenoid current ramps down during the shot, this fringing field changes and influences the divertor region field. As the strike point sweeps the divertor target plates, each probe records the variation around the strike point region. The motion of the strike point is depicted in Fig. 4. The ion saturation current density, recorded at a frequency of 1 MHz is shown on six divertor target tips, three on the low and three on the high-field side (for the tip numbers see Fig. 2). The strike point motion from one probe tip to the other is clear in the way the shape of the strike point region is shifted in time. This enables us to convert time to spatial dependence because the strike point velocity is slow compared to the turbulent fluctuations time scales. Taking into account the distances between probes (20 and 6 mm for the low- and high-field sides, respectively), one can deduce that the velocities of the outer-lower and inner-lower strike points are ≈ 2.7 and 0.7 m/s. The strike point sweep enables us to determine the properties of turbulence around the strike point using only one tip; the other tips are used hereafter to accumulate data for statistical analyses.

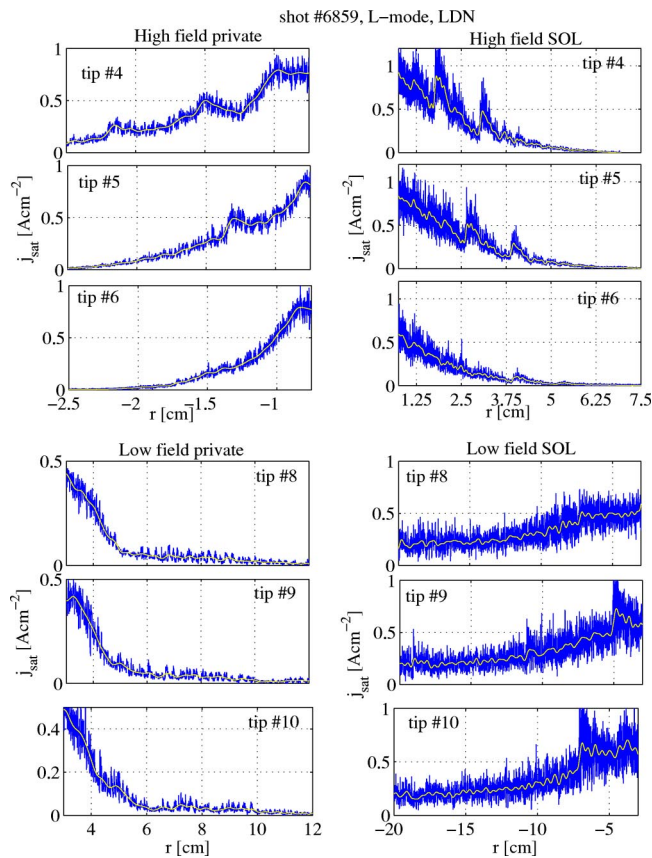


FIG. 5. Details of the four regions, namely, high- and low-field SOL and high- and low-field private regions, using three probe tips. Also shown is the low-frequency component of the signals in order to emphasize the absence of high intensity fluctuations with respect to the mean values for all positions.

Once the time-to-space conversion is made, Fig. 5 shows the radial profile of the ion saturation current at the target plates. In Fig. 5, r denotes the distance to the strike point chosen to be the origin. The strike point is estimated as corresponding to the maximum of the low frequency component of j_{sat} . The data are from shot number 6859 with a single lower null configuration. The four regions investigated are the low-field SOL, the low-field private flux, the high-field SOL, and the high-field private flux. Moreover, and in order to show the reproducibility of the results, we plotted for each region the j_{sat} taken on three different probe tips. In Fig. 5, we superposed on the raw j_{sat} curves their average values. In contrast to what was shown at the midplane, the fluctuations are most of the time about the average values with approximately equal probability to have positive and negative values. Consequently, it is rather straightforward to show that an exponential dependence on r of the four regions is a good approximation of the various radial profiles which is in agreement with the figures given in Ref. 26.

C. Comparing the target probes signals

Now that we have shown the raw signals at the different poloidal locations and as a function of the distance to the strike point, we aim at giving a more quantitative comparison by using statistical methods. For each signal, we subdi-

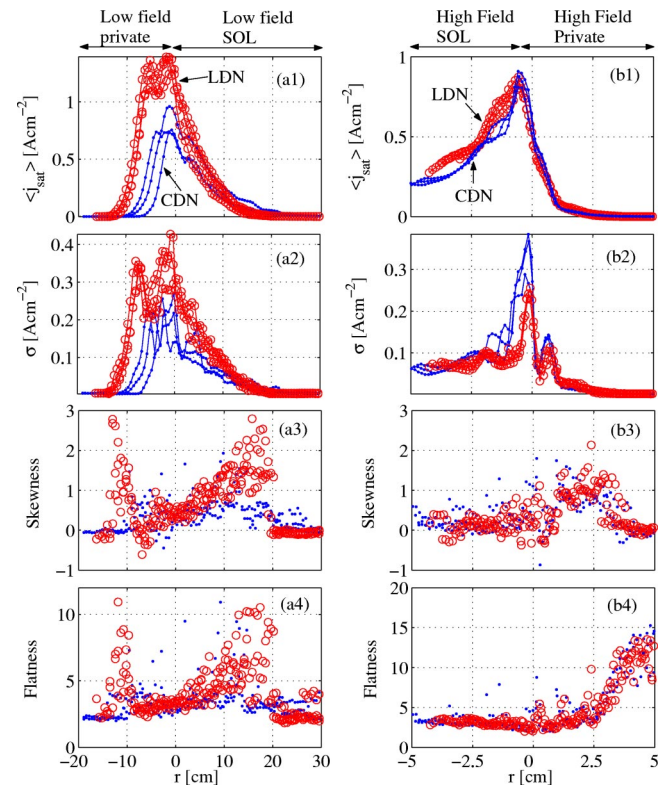


FIG. 6. (a1)–(a4) describe for the low-field target probes, respectively, the average value of j_{sat} , the standard deviation σ , the skewness $(\langle \tilde{j}_{\text{sat}}^3 \rangle / \langle \tilde{j}_{\text{sat}}^2 \rangle^{3/2})$, and the flatness factors $(\langle \tilde{j}_{\text{sat}}^4 \rangle / \langle \tilde{j}_{\text{sat}}^2 \rangle^2)$ as a function of the distance to the strike point; The tilde denotes the fluctuation part of the ion saturation current densities ($\tilde{j} = j_{\text{sat}} - \langle j_{\text{sat}} \rangle$). The single null (\circ) as well as the double null (\cdot) magnetic configurations are shown. The same quantities and symbols are used in (b1)–(b4) for the high-field divertor target probes.

vide the time series into blocks of 10 000 points overlapping by 3000 points. The stationary condition breaks down only when the standard deviation change occurs at time scales shorter than 10 ms. When this happens the corresponding statistical values will be disregarded.

The average values of the ion saturation current density are shown in Figs. 6(a1) and 6(b1). The different regions that are probed are inserted on the top of (a1) and (b1). Accordingly, the negative values of r denote here the low-field private and the high-field SOL for both LDN and CDN discharges. In L -mode plasmas, it appears that operating in CDN with respect to LDN does not have any affect on the overall (parallel) particle flux nc_s on the high-field side of the tokamak as subplot (b1) indicates. However, on the low-field side, the particle flux at the strike point is divided approximately in half reflecting a smaller particle load. It has been shown that the other half is collected at the upper divertor region.²⁸

In Figs. 6(a2) and 6(b2) is plotted the standard deviation σ of j_{sat} fluctuations where the average value is set equal to 0. The level of fluctuations on the low-field side is higher in the LDN than in the CDN configuration. This could explain the average value increase in (a1) as in this region the main source of particles is radial transport. On the high-field side, little changes are recorded between the two magnetic configurations.

The skewness and the flatness factors are the two main statistical tools that are used in this paper to assess the role of avaloids. They are defined as the third- and fourth-order moments of the j_{sat} fluctuations normalized by the standard deviation. As it was shown on different occasions,^{13,14} avaloids lead to both a positive skewness factor and a flatness factor significantly greater than 3. The skewness factor of a Gaussian signal is equal to 0 reflecting the same probability to have positive or negative fluctuations around the average value. Also in the Gaussian case, the flatness factor is equal to 3 quantifying the weight of the tails with respect to the core of the distribution.

In subplots (a3) and (b3) of Fig. 6, the skewness is shown as a function of r the distance to the strike point. The flatness factor is in (a4) and (b4). The deviation of the probability distribution function (PDF) from Gaussian on the high-field side occurs only in the private region at $r > 2.5$ cm. In this region, the average value shown in (b1) is approximately zero and the standard deviation is low reaching the noise level value. Moreover, the deviation is recorded on the flatness factor alone, the skewness factor being still around 0. Hence, this deviation reflects the non-Gaussian character of the instrumentation noise and not the properties of the flow.

On the low-field private region at $r \sim -10$ cm, the deviation is recorded on both the skewness and the flatness factors. However, the deviation of both quantities from Gaussian values takes place where the average value of j_{sat} decreases sharply. A closer look at the data indicates that this is caused mainly by the nonstationarity of the signals.

The only region where a systematic deviation from a Gaussian is recorded is in the low-field side of the SOL ($0 < r < 20$ cm). This is consistent with the measurements at the low-field midplane. The skewness and the flatness factors deviate from 0 and 3, respectively, as r increases. The skewness factor reaches ≈ 2 , whereas the flatness factor is about 8 at $r \approx 15$ cm. Because of the field lines expansion, this distance is equivalent to about 3 cm at the midplane. This deviation stops at $r \approx 20$ cm where the average value goes to 0, the standard deviation reaches the instrumental noise level and the flatness and skewness factors are that of Gaussian values. This sudden change in the statistical properties of turbulence is caused by the presence of the P3a and P3b magnetic coils; P3a and P3b were illustrated in Fig. 2. They intercept the field lines making the parallel connection length much smaller and thus intercepting most of the particle and heat fluxes.

D. Comparing the low-field fluctuations at the midplane and at the divertor target

In consequence of the results described above, a particular attention is paid to the comparison between turbulence at the low-field midplane and the divertor target plates SOL. This is illustrated in Fig. 7 where the average value, the standard deviation, the skewness, and the flatness factors are plotted against r which denotes the distance to the LCFS for the midplane probe and the distance to the strike point for the target probes. As stated earlier, the distance of 30 cm away

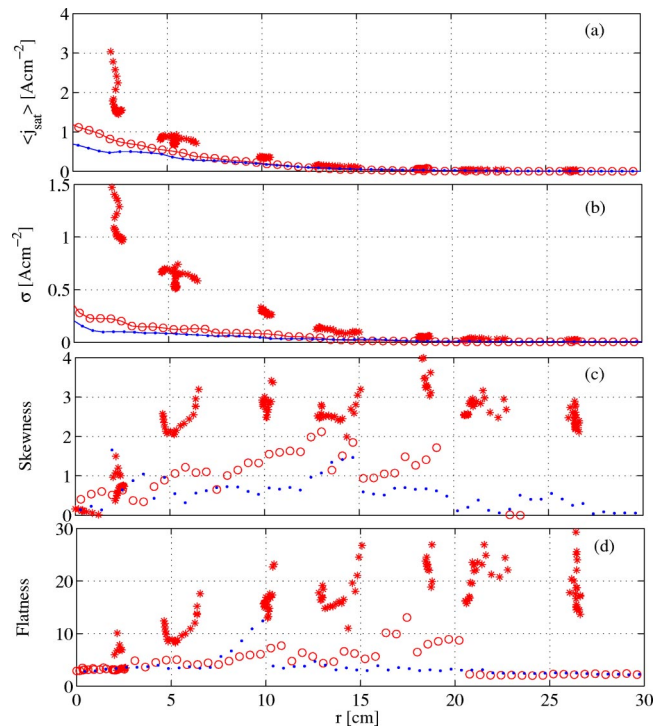


FIG. 7. Comparison of the fluctuations statistical properties recorded at the midplane and the low-field divertor target using the reciprocating and the target probes. The symbols (\cdot) and (\circ) represent the CDN and LDN configuration, respectively, for the target probes. The asterisks ($*$) represent the midplane properties obtained from the five shots (6852, 6853, 6854, and 6856). In (a)–(d) are illustrated, respectively, the average value, the standard deviation, the skewness factor, and the flatness factor as a function of r which denotes the distance to the LCFS for the RP and the distance to the strike point for the target probes. Due to the field line expansion in the target region, the distance of 30 cm away from the strike point is equivalent to 6 cm away from the last closed flux surface.

from the strike point is connected to a position about 6 cm from the LCFS at the midplane. The data at the midplane is obtained from the four shots 6852, 6853, 6854, and 6856 in the time period between 0.25 and 0.3 s (see Fig. 1) where the density is assumed constant in addition to the other plasma properties such as the plasma current. It is mainly the uncertainty about the reciprocating probe position that leads to the observed error bars in Fig. 7.

Near the LCFS, the parallel particle flux nc_s is approximately four times higher at the midplane than at the target. This large difference cannot be caused by avaloids alone as it has been shown that about 50% of the transport is caused by convective structures.^{13,14} This brings the ratio of the parallel particle fluxes at the midplane and the divertor target down to 2. Other mechanisms have thus to be included, mainly the effect of the magnetic shear on turbulence which is the main source of particles outside the separatrix.

Figure 7(b) indicates that turbulence intensity at the midplane is approximately five times bigger than at the target plates. Since the main source of particles in the SOL is radial transport from the plasma edge, the asymmetry of the average particle flux values is consistent with that of the turbulence fluctuations intensity.

When the positions are renormalized to take into account the field lines expansion at the target region, the flatness and

skewness values are found similar from both the TPs and the RP. However, a closer look at the data at the TP, that can be seen in Fig. 5, indicates that the deviation from Gaussian distribution is not caused by bursts. It appears as if positive fluctuations have higher values than negative fluctuations. This is consistent with the idea that avaloids at the midplane, that are radially and poloidally localized, are spread radially due to the field lines expansion. Therefore, their bursty signature is not clearly visible because their intensity is now spread over a wide region, but they still lead to a deviation from a Gaussian distribution. The connection between plasma at the midplane and at the target is done via the field lines.

In conclusion, the turbulent fluctuations in the private flux regions and at the high-field side are reported to be rather Gaussian reflecting the absence of avaloids. At the low-field side, however, turbulence is non-Gaussian both at the midplane and at the target plates with intermittency increasing with the distance to the separatrix and the LCFS. At the midplane intermittency is caused by bursts. At the target plate, it is caused by an asymmetry in the fluctuations amplitude. The difference is caused by the field line expansion mainly between the X point and the target plates which decreases the effect of the midplane bursts by spreading the perturbation radially over large distances.

IV. PROPERTIES OF AVALOIDS BY IMAGING

To link the properties of turbulence on the low-field side occurring between the midplane and the target, we use a fast imaging camera. Two exposure times are used, 10 and 195 μs . The frame rate, being of the order of a few thousand frames per second, is in both cases slow with respect to the evolution of turbulent structures. Therefore, consecutive images are independent snap shots. The images are caused by the D_α light naturally coming from the plasma without the use of localized gas puffing.

A. ELM-free Ohmic H -mode plasma reference picture

Before we start investigating L -mode plasmas with discharge properties similar to the ones discussed earlier using the probes, we show Fig. 8 where the plasma is in an ELM-free Ohmic H -mode state (shot 6864). The exposure time is 10 μs . The last closed flux surface can be clearly seen in form of a quasircular narrow region that separates the main plasma from the SOL. Also visible is the upper X point where plasma appears to have higher density judged from the higher level of light emitted with respect to the LCFS light intensity. Also can be seen in this figure is the center stack and the region where gas is injected into the plasma for fueling. The fueling causes the red spot in the bottom left of the figure. Figure 8 serves as a reference to the L -mode pictures that are going to be discussed hereafter.

B. Images with 10 μs exposure time

The pictures are deduced from a plasma discharge (6864) where only Ohmic heating is present. The discharge starts in L mode before the plasma switches into an Ohmic

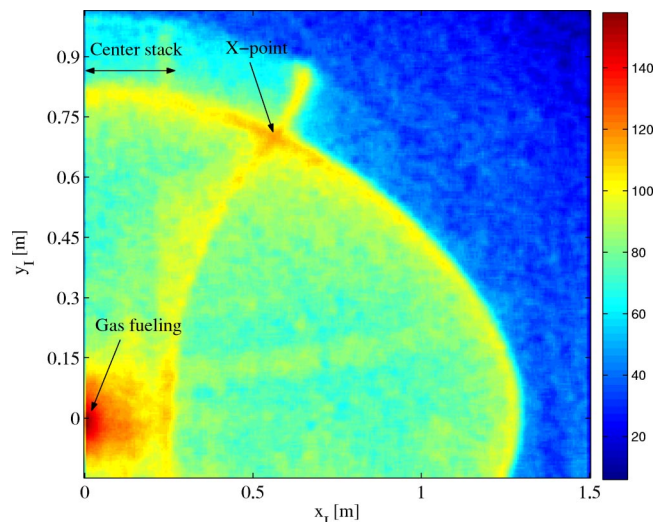


FIG. 8. Image displaying the D_α light coming from an Ohmic H -mode plasma (shot 6863) using the Phantom V4 fast camera. In the image one can see the center stack, the X point and the high-field side gas fueling region rather clearly. Note the sharp region separating the plasma edge from the scrape-off layer. x_I and y_I describe approximately the axis of the image and the origin is chosen to be at the middle of the center stack.

H -mode regime. This shot is in double null configuration. Figure 9 illustrates four sample pictures taken at arbitrary times with a resolution of 256×256 . Viewing an area approximately of about 1 m^2 leads to a subcentimetric resolution. However, other factors lead to the decrease of the effective resolution such as poloidal and/or toroidal rotation and spatial integration. A radial velocity of 1 km/s (Ref. 14) leads a smearing of about 1 cm. Accordingly, it is safe to say that the resolution of the images is of the order of 1 cm. Light results from D_α emission and the intensity scale is the same for the four pictures. The region between closed and open field lines is not a sharp boundary near the LCFS as in Fig. 8, but consists of a wide region that extends on both sides of the separatrix. In order to make this issue clearer, we

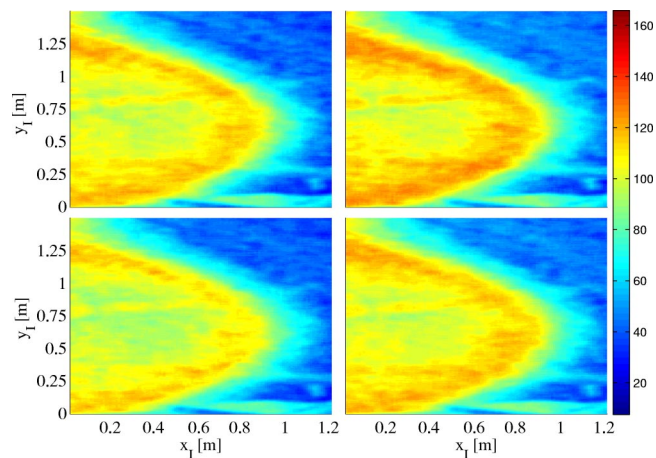


FIG. 9. Four sample images from the Phantom V4 camera of an L -mode plasma (shot 6863) taken at arbitrary times. The x_I and y_I are approximate spatial dimensions of the image. Note that the plasma edge is very different to that in the H -mode case. The D_α light is strongly modulated both in the poloidal and the radial directions. The four images have the same color scale.

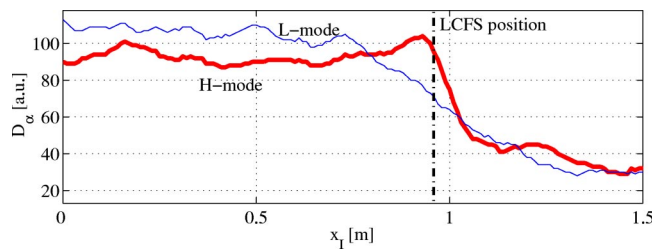


FIG. 10. A radial cut through the pictures taken for *L*- and *H*-mode plasmas. Note the steep gradient of the *H*-mode trace (in thick solid line) and the shallower one in *L* mode (solid line). The approximate position of the LCFS is indicated with a vertical dash-dotted line.

plotted in Fig. 10 two radial profiles of the D_α light. In *H* mode the gradient near the LCFS is four times greater than in *L* mode where the light intensity continuously decreases starting from inside the separatrix to the open field line region. This rough estimate of the gradient changes agrees with a more sophisticated method where the light intensity is unfolded taking into account the emissivity profile.²⁹

In Fig. 9, ripples near the separatrix caused by patches of a high level of fluctuations can be seen. Because, these fluctuations have large scales, we believe that they are images of avaloids. Two reasons are behind the fact that it is hard to see them detach from the main plasma. The first is the temperature decrease as they propagate radially outward leading to a strong decrease of their D_α light emission. The second reason is their toroidal extension along the field lines and the camera tangential view. Hence, avaloids will still appear to be attached even when they are not.

In order to emphasize the fluctuations independently of the background we applied a two-dimensional high-pass “Direct Form II Transposed” filter to remove the large-scale components of the image above ≈ 10 cm. The result is shown in Fig. 11. The objects present inside the vacuum

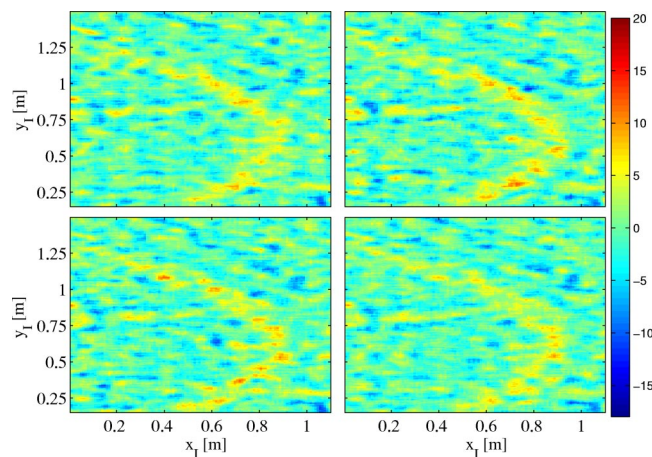


FIG. 11. The four images of Fig. 9 (shot 6863) are replotted after filtering out the large-scale component. Avaloids appear as high intensity (in red) and large-scale structures that extend from the open to the closed field line regions. The four images have the same color scale. The features that are common to the four images, for example, a horizontal line in the middle, result from fixed objects in the tokamak that were not removed by the filters. This is caused by the fact that these structures have spatial scales that are of the order or smaller than the fluctuations scales.

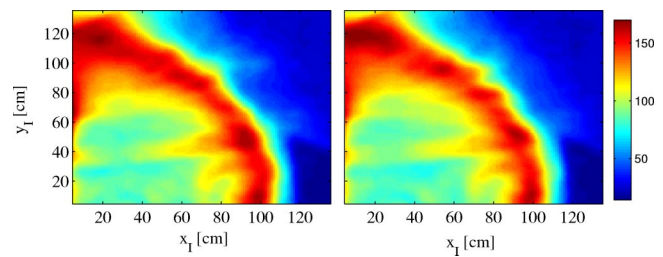


FIG. 12. Two sample images from the Phantom V4 camera of a plasma in *L* mode (shot 4918) with $195 \mu\text{s}$ exposure time. The x_I and y_I are approximate spatial dimensions of the image.

vessel reflecting the plasma light with scales about the macroscales of turbulence and thus smaller than the bandpass of the filters give rise to the features that are present in all of the figures. Poloidally and radially localized structures are thus more clearly visible in the four pictures around the separatrix. They exist mainly in the vicinity of the separatrix. Their typical scale is ≈ 5 – 10 cm. Moreover, the fluctuations seem to be modulated with a given poloidal wave number as the top right-hand plot of Fig. 11 indicates. This suggests the existence of an instability with a high poloidal wave number. Similar results were obtained in linear devices¹⁵ where a saturation of an edge instability was shown to be the origin of the bursts. From the four pictures, one can notice a poloidal asymmetry in the distribution of the fluctuations. Close to the divertor region, and near the *X* point, fluctuations appear to have a lesser amplitude even though more light is recorded in this region.

C. Images with $195 \mu\text{s}$ exposure time

In order to increase the signal-to-noise level, we use another set of pictures with a longer exposure time equal to $195 \mu\text{s}$. A sample of two pictures is shown in Fig. 12 where the same type of structures and ripples around the separatrix as in Fig. 9 exists. However, one might wonder that with this large integration time and the supposed large radial and poloidal velocity of avaloids, one would expect a strong signature of smearing. The reason why structures are still rather clearly visible is because the smearing length scale is determined not only by the camera shutter time but also the D_α emission lifetime (with intensity greater than the camera noise level). The other fact that comes into play is the time between bursts which is about $200 \mu\text{s}$.¹⁴ As avaloids radially propagate into the SOL at a speed about 10^5 cm/s,¹⁴ the temperature and density drop due to parallel connection to the divertor plates. If one assumes that the temperature decrease occurs within the SOL decay length that is about few centimeters in MAST, then one can estimate the lifetime of the D_α emission to be roughly of the order of $50 \mu\text{s}$. Consequently, increasing the shutter opening time above this value would not modify significantly the images. However, once the integration time is greater than $200 \mu\text{s}$, then several avaloids are included in one picture and more smearing takes place.

In order to obtain the fluctuations, we subtract not only the low wave-number component of each picture but also the

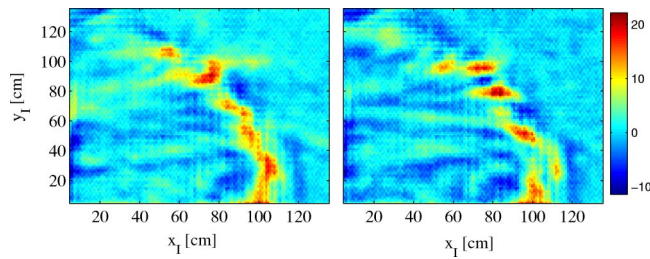


FIG. 13. The two images of the previous figure (shot 4918) are replotted after subtraction of the background and the large-scale component. The exposure time is $195 \mu\text{s}$. Avaloids appear clearly as high intensity and large-scale structures that extend from the open to the closed field line regions. The two images have the same color scale.

background as it contains fine structures that interfere with the turbulent structures. The background is obtained by averaging over 50 consecutive images. This number is limited by the stationary conditions of the discharge, mainly that of the average density which increases in time. The result is illustrated in Fig. 13, where the striations of the background almost disappeared. In Fig. 13 elongated structures that stretch between the closed and open field lines are clearly seen. Moreover, and in agreement with the $10 \mu\text{s}$ exposure time images, the structures are large scale (5–10 cm) and are localized in both the radial and poloidal directions. Another point of agreement with the $10 \mu\text{s}$ pictures is that fluctuations around the separatrix seem to possess some periodicity in the poloidal direction.

D. Fluctuations properties around the low-field separatrix

In order to investigate the properties of fluctuations around the separatrix in a more comprehensive way, a curve is selected about which the dependence of the fluctuations as a function of time is recorded. The curve is illustrated by a thick black solid line in Fig. 14. The idea here is to show that the two pictures of Fig. 13 are not some special cases but represent the usual behavior of fluctuations around the separatrix. The dependence on time depicted in Fig. 14 shows that the bursty behavior of the D_α fluctuations takes the form of “hills” localized in the poloidal plane. This figure shows that avaloids are present at all poloidal angles on the low-field side with different amplitudes. When the selection curve reaches the area around the X point the level of fluctuations is observed to decrease.

We now aim at determining the poloidal correlation of the fluctuations that occur on the curve represented in Fig. 14. One difficulty that is encountered in deducing statistical values is that the images are not correlated and the length of the curve where the fluctuations are selected is rather small in which only a few events can take place. To overcome these difficulties, we choose a reference point (called point 1) on the analyzed curve (the one parallel to the separatrix) and record its light intensity as well as the light intensity at another point (called point 2). This is done for all the frames in time. Then, the two intensities are plotted one with respect to the other and the slope of the curve is calculated. If the slope is about 0, this means that there is no correlation between the

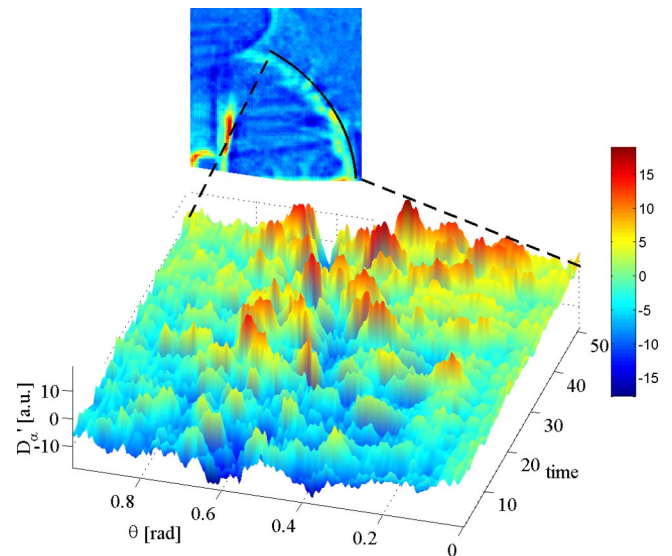


FIG. 14. The top figure shows the plasma image and a curve selected slightly outside the LCFS represented in thick black solid line. The bottom figure shows the plot of the D_α fluctuations (D_α') of the light occurring on that curve as a function of the poloidal angle and time. The time unit is $1/3731$ s. Note that fluctuations appear in bursts with some poloidal scale. Note also that the level of fluctuation decrease as the investigated region is close to the X point. The decrease of the level of fluctuations at $\theta \sim 0$ is caused by the existence of an antenna which is blocking the light coming from the SOL.

light intensities at the two points. If it is about 1, it reflects that whenever high or low intensity occurs at the reference point it also occurs at point 2. In Fig. 15(a), we plot the dependence of the light intensity fluctuations of a reference point with respect to the D_α fluctuations at two points with different poloidal angles; the stars denote the case where the second point is close to the reference, and the circles when they are far apart. The linear fit of both graphs is shown in dashed and dash-dotted lines, respectively. The slope of the lines is denoted by ξ and plotted in Fig. 15(b) as a function of the poloidal angle θ for two reference points. The result indicates that the correlation is local in the poloidal direction and gives statistical confirmation to the behavior shown in Fig. 14. The length-scale associated with the poloidal corre-

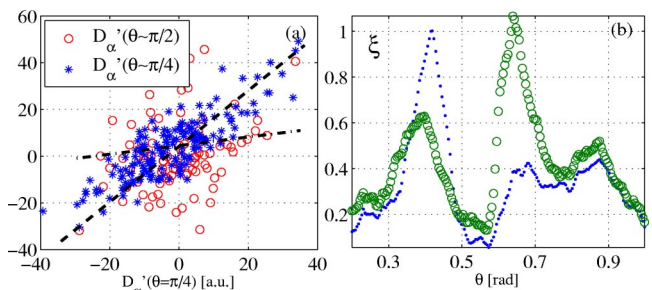


FIG. 15. (a) Shows the D_α fluctuations at a point in the SOL near the LCFS as a function of another point at the same radius but a different poloidal angle. The asterisks denote the case where the two points are spatially close and the circles the case where they are far apart. The slope of the best fit ξ is represented by ξ . In (b) ξ is shown as a function of the poloidal angle θ for two reference points at poloidal positions about 0.4 and 0.65 rad. The poloidal correlation scale is about 5 cm.

lation is about 5 cm. It is of the same order as the radial scale length found on MAST using electric Langmuir probes.¹⁵

In conclusion, we used in this section a fast camera taking images at 10 μ s time scale in order to investigate the poloidal distribution of D_α fluctuations. We showed images of structures that are several centimeters in diameter that can be the avaloids investigated in the previous section using Langmuir probes. These results were corroborated by images with longer integration time where the signal-to-noise ratio is higher. The LCFS is found wavy with large structures that can extend from the closed to the open field lines. Avaloids are found on the low-field side with asymmetric poloidal distribution in agreement with the results obtained using electrical probes.

V. DISCUSSION

Using Langmuir probe mounted around the vacuum chamber in MAST and a fast imaging camera, we showed that while bursts, the signature of avaloids, are clear at the midplane, they are nearly absent at the different target plates. We recall that avaloids are defined as large-scale structures with high radial velocity encountered intermittently in the scrape-off layer.¹³

Fluctuations at the target plates and at the midplane were acquired at an acquisition frequency equal to 1 MHz. The motion of the strike point at a constant velocity enabled us to convert time into position with respect to the strike point. At the midplane, plasma is shown to exist as far as 30 cm away from the LCFS in an intermittent fashion. Moreover, the properties of turbulence at the midplane are highly non-Gaussian as the skewness and flatness factors reach, respectively, 3 and 20 at $r \approx 7$ cm. As it is now understood, the non-Gaussian character and the fact that plasma is found far from the region where it is being produced are intimately linked to avaloids. The link between the midplane plasma and that at the target is done by the field lines.

The difference in the signal statistical properties of turbulence measured at the midplane and at the low-field divertor target is mainly caused by the field lines expansion at the target that is intrinsic to the divertor magnetic configuration. In MAST, and as it was shown in Fig. 2 the target plates are installed far from the X point leading to considerable field line expansion in the radial direction. Consequently, a 5 cm structure of plasma at the midplane would expand to cover the whole 30 cm at the target. The burst in the ion saturation current at the midplane would lead to a rather small increase of the overall level of j_{sat} at the target as the power and particles are distributed over a larger area. In addition to field line expansion and in order to explain the difference in the particle flux recorded at the midplane and at the target, we emphasize the role of magnetic shear as a parameter that, locally around the X point, might suppress turbulent fluctuations.

On the low-field side, having a detailed radial profile of the fluctuations at the midplane and at 12 different target probes, we performed the cross correlation between the two signals. First, we divide the time series recorded on the RP and TP into nonoverlapping sections of 10 ms duration.

Then, we recorded the cross-correlation amplitude, between any of the sections on the RP and any of the section on a TP; this leads to a matrix of 18×18 . This process is repeated for all the 12 target probes and for the 5 shots (6852, 6853, 6854, 6856, and 6857) where the RP position is changed. When this is done, in all, the cross-correlation amplitudes of 19 440 cases are studied. No cross correlation above the noise level was observed between any of the time series sections. The reason for this is the three-dimensional character of avaloids as they are filaments localized in the radial, poloidal, and toroidal directions.

On the low and high field sides of the private region, the fact that intermittent bursts do not occur has a different origin. The private plasma is formed of only open field lines and its connection to the plasma is through the X point. Accordingly, the X -point complex magnetic structure dominates the presence of oscillations and/or turbulent fluctuations in this region.^{30–32} Let us assume that to the lowest order one has $\vec{k} \cdot \vec{B} = 0$ this leads to a relation between the poloidal and the toroidal wave numbers that reads $k_\theta = nB_\phi / RB_\theta$.³³ The plasma major radius is R , n is the toroidal mode number, B_ϕ and B_θ are the toroidal and poloidal magnetic fields, respectively, and k_θ is the poloidal wave number. Around the X point B_θ tends to 0 leading to $k_\theta \rightarrow \infty$ or to $n \rightarrow 0$. In other words, turbulent fluctuations or coherent oscillations are usually damped by viscosity because of the small poloidal scales. In the case where poloidally extended structures exist near the X point, they should have very long toroidal connection length. This makes drift wave as well as other types of instabilities more stable. In addition, regions inside the separatrix near the X point possess a high level of magnetic shear that suppresses instabilities and turbulence.^{34–36} Hence, different effects make the private plasma region rather stable with respect to many types of instabilities including the Rayleigh–Taylor one which is thought to be behind avaloids generation.

In the high-field side of the scrape-off layer, the fact that intermittency is not recorded is reflective of the effect of good curvature on the instabilities and turbulence. The measurements presented here were made at the target and not at the midplane. But as we saw with the low-field side measurements, the two areas are connected by the field lines. However, the effect of field lines expansion at the high-field side is much smaller than at the low-field side. Hence, one would expect a higher correlation between the midplane and the target at the high with respect to the low-field side of the tokamak.

The overall picture that one ends up with on the basis of the experimental results presented in this paper is in good agreement with the numerical simulation using the BOUT code simulating DIII-D discharges.^{31,32} Turbulent fluctuations are observed to be poloidally asymmetric and actually rather localized on the low-field side. As discussed above different mechanisms enter into play to give rise to this asymmetry.

ACKNOWLEDGMENTS

This work was performed under the U.S. Department of Energy under Contract No. DE-FG03-95ER-54301 and was jointly funded by Euratom and the UK Engineering and Physical Sciences Research Council.

- ¹S. J. Zweben and R. W. Gould, Nucl. Fusion **25**, 171 (1983).
- ²R. Jha *et al.*, Phys. Rev. Lett. **69**, 1375 (1992).
- ³M. V. A. P. Heller *et al.*, Phys. Plasmas **6**, 846 (1999).
- ⁴V. Carbone, G. Regnoli, E. Martines, and V. Antoni, Phys. Plasmas **4**, 445 (2000).
- ⁵M. A. Pedrosa *et al.*, Plasma Phys. Controlled Fusion **38**, 365 (1996).
- ⁶T. L. Rhodes *et al.*, Phys. Lett. A **253**, 181 (1999).
- ⁷B. Ph. Van Milligen, C. Hidalgo, and E. Sanchez, Phys. Rev. Lett. **74**, 395 (1995).
- ⁸R. Jha and Y. C. Saxena, Phys. Plasmas **3**, 2979 (1996).
- ⁹A. V. Filippas *et al.*, Phys. Plasmas **2**, 839 (1995).
- ¹⁰B. A. Carreras *et al.*, Phys. Plasmas **5**, 3632 (1998).
- ¹¹G. D. Wang, G. Antar, and P. Devynck, Phys. Plasmas **7**, 1181 (2000).
- ¹²G. Antar, P. Devynck, X. Garbet, and S. C. Luckhardt, Phys. Plasmas **8**, 1612 (2001).
- ¹³G. Y. Antar *et al.*, Phys. Rev. Lett. **87**, 065001 (2001).
- ¹⁴G. Antar *et al.*, Phys. Plasmas **10**, 419 (2003).
- ¹⁵G. Antar, Phys. Plasmas **10**, 3629 (2003).
- ¹⁶U. Firsch, *Turbulence: The Legacy of A. N. Kolmogorov* (Cambridge University Press, Cambridge, 1995).
- ¹⁷A. K. M. F. Hussain, J. Fluid Mech. **173**, 303 (1986).
- ¹⁸P. Holmes, J. L. Lumley, and G. Berkooz, *Turbulence, Coherent Structures, Dynamical Systems and Symmetry* (Cambridge University Press, Cambridge, UK, 1996).
- ¹⁹D. L. Rudakov *et al.*, Plasma Phys. Controlled Fusion **40**, 717 (2001).
- ²⁰S. I. Krasheninnikov, Phys. Lett. A **283**, 368 (2001).
- ²¹H. Zohm, Plasma Phys. Controlled Fusion **38**, 1213 (1996).
- ²²G. R. Tynan, J. Liberati, R. J. Taylor, and B. Wells, Plasma Phys. Controlled Fusion **38**, 1301 (1996).
- ²³C. Fenzi *et al.*, Plasma Phys. Controlled Fusion **38**, 1043 (1999).
- ²⁴A. Sykes *et al.*, Phys. Plasmas **8**, 2101 (2001).
- ²⁵L. L. Lao *et al.*, Nucl. Fusion **30**, 1035 (1990).
- ²⁶J.-W. Ahn and G. F. Counsell, J. Nucl. Mater. **290-293**, 820 (2001).
- ²⁷G. F. Counsell *et al.*, Plasma Phys. Controlled Fusion **44**, 827 (2002).
- ²⁸A. Kirk *et al.*, Plasma Phys. Controlled Fusion **46**, 551 (2004).
- ²⁹M. R. Tournianski *et al.*, Rev. Sci. Instrum. **74**, 2089 (2003).
- ³⁰D. Farina, R. Pozzoli, and D. D. Ryotov, Nucl. Fusion **33**, 1315 (1993).
- ³¹X. Q. Xu *et al.*, Nucl. Fusion **40**, 731 (2000).
- ³²X. Q. Xu *et al.*, Nucl. Fusion **42**, 21 (2002).
- ³³J. R. Myra, D. A. D'Ippolito, X. Q. Xu, and R. H. Cohen, Phys. Plasmas **7**, 2290 (2000).
- ³⁴B. Bhattacharayya, Phys. Fluids **29**, 2210 (1986).
- ³⁵M. Nadeem, T. Rafiq, and M. Persson, Phys. Plasmas **8**, 4375 (2001).
- ³⁶A. Kendl and B. D. Scott, Phys. Rev. Lett. **90**, 035006 (2003).